Enhanced Quantitative Wavefront Imaging for Nano-Object Characterization

Clémence Gentner, Benoit Rogez, Hadrien M L Robert, Anis Aggoun, Gilles Tessier, Pierre Bon, Pascal Berto

ACS NANO

www.acsnano.org

ARTICLE

Enhanced Quantitative Wavefront Imaging for Nano-Object Characterization

Clémence Gentner,[#] Benoit Rogez,[*,#] Hadrien M. L. Robert, Anis Aggoun, Gilles Tessier, Pierre Bon, and Pascal Berto[*]

Cite This: https://doi.org/10.1021/acsnano.4c05152

Read Online

ACCESS | Metrics & More | Article Recommendations | Supporting Information

ABSTRACT: **Quantitative phase imaging enables precise and label-free characterizations of individual nano-objects within a large volume, without *a priori* knowledge of the sample or imaging system. While emerging common path implementations are simple enough to promise a broad dissemination, their phase sensitivity still falls short of precisely estimating the mass or polarizability of vesicles, viruses, or nanoparticles in single-shot acquisitions. In this paper, we revisit the Zernike filtering concept, originally crafted for intensity-only detectors, with the aim of adapting it to wavefront imaging. We demonstrate, through numerical simulation and experiments based on high-resolution wavefront sensing, that a simple Fourier-plane add-on can significantly enhance phase sensitivity for subdiffraction objects—achieving over an order of magnitude increase (×12)—while allowing the quantitative retrieval of both intensity and phase. This advancement allows for more precise nano-object detection and metrology.**

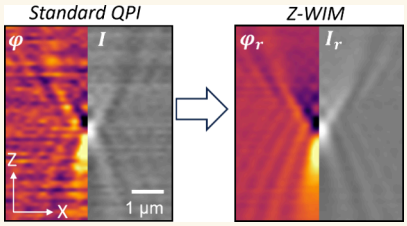

KEYWORDS: *quantitative phase imaging, sensitivity increase, nanoparticles, scattering contrast, single nano-object metrology*

The precise detection and characterization of individual nano-objects are of paramount importance across various fields of science, including physics, chemistry, biology, and medicine. In physics and chemistry, the synthesis, transformation, and use of nanostructures and nano-optics are a hot topic.[1] Concurrently, biological nano-objects such as viruses and vesicles are attracting more and more attention in medicine not only for the comprehension of viral processes[2] but also for nanomedicine applications.[3] As nanoparticles (NPs) find broader applications in fields such as cosmetics and food additives,[4] and with the surge in clinical trials utilizing nanocarriers,[5,6] versatile and effective quality control methodologies become increasingly vital.[7,8] Extensive efforts have been made over the past decade to develop simple, non-invasive, label-free imaging methods capable of detecting NPs with extreme sensitivity.[9−11] However, it remains challenging for most strategies based on intensity measurement to provide enough specific information to accurately characterize a mixture of unknown nano-objects, e.g., water pollutant determination,[12,13] without *a priori* knowledge of their composition and properties.

In this context, quantitative phase imaging (QPI) recently emerged as a powerful method for NP characterization. By giving access not only to the amplitude of the electromagnetic (EM) field but also its phase, QPI—often performed with a digital holographic setup—offers numerous advantages over intensity-only methods including numerical refocusing,[7,14] numerical aberration correction,[15] sensor dynamic optimization,[16,17] and metrology without *a priori* knowledge about the sample.[17−24] In particular, QPI enables the precise estimation of the complex optical polarizability, thereby providing insights into the absorption and scattering cross sections independently of the NP's shape or composition.[21] In, e.g., biological applications, this allows us to determine the dry mass of biological objects.[7,25] Importantly, this approach bypasses any need for sample calibration, assumptions about sample composition, and any prior knowledge of the optical system. An important feature of QPI in assessing nanoparticle concentrations lies in its ability to analyze large volumes through numerical refocusing of the EM field.[16,26−28] Instead of being limited to a surface or its close vicinity, this allows the in situ characterization of moving NPs in solutions, i.e., dispersed in 3D. Incidentally, numerical refocusing and single NP (super)localization also allow accurate hydrodynamic sizing by leveraging Brownian motion analysis along extensive, 3D trajectories. Based on such analyses, several recent works have demonstrated the potential of QPI to estimate the mass or chemical nature of unknown NPs, viruses, or vesicles in solution and even identify them in a label-free manner.[17,22,23] A recent

Received: April 18, 2024
Revised: June 7, 2024
Accepted: June 12, 2024

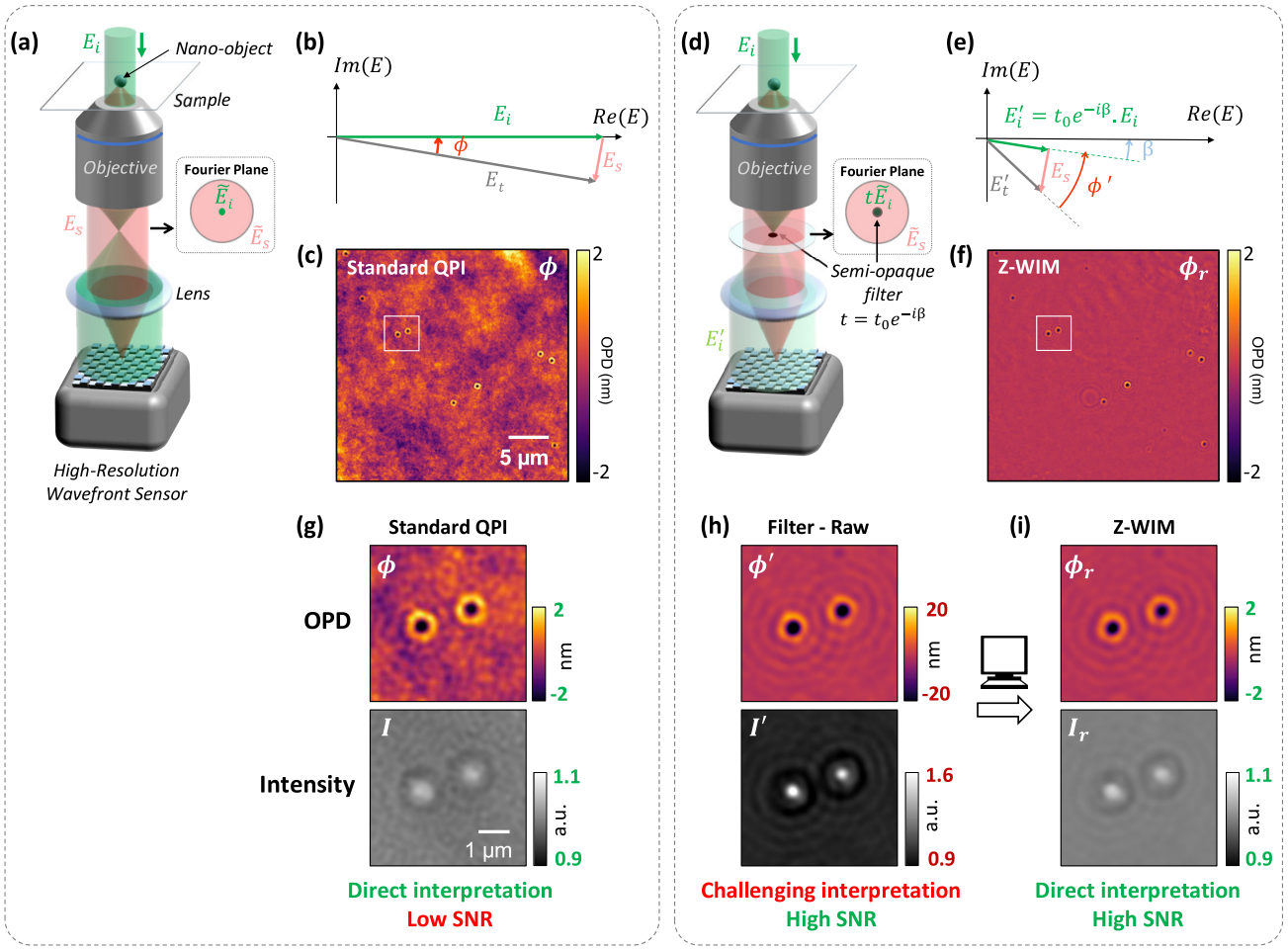

Figure 1. Schematics of the experimental configuration in (a) standard common-path QPI (represented here as a classical QLSI implementation) and (d) Z-WIM. (b) Complex plane representation of the incident (E_i), scattered (E_s), and transmitted (E_t) fields in the image plane. (e) Complex plane representation with the Z-WIM setup. (c, f) Phase images of 100 nm-diameter polystyrene NPs on glass in water for each configuration and (g–i) zoom on the phase and intensity images of an NP (g) in standard QPI and (h) before and (i) after numerical reconstruction, showing the sensitivity gain and the quantitativity (note the identical color bars in g and i) of Z-WIM.

study has even demonstrated the ability to characterize nano-objects down to the scale of a single protein, albeit at the cost of increased experimental complexity.[29]

The main roadblock to the detection of weak scattering/extinction cross sections from single nano-objects arises from the very little amount of light scattered when compared to the nonscattered light. The limited dynamics of detectors, especially cameras, precludes the detection of the smallest particles. To effectively enhance detection capabilities, the dominant strategy relies on an optimal use of this limited dynamics by (i) rejecting most of the illumination light while preserving the scattered light to avoid detector saturation and (ii) exploiting the gain provided by a coherent reference field to achieve a signal level significantly above the readout noise.[30−33] Implementing these can be straightforward in interferometric techniques using an external reference arm, like digital holographic microscopy: on the measurement arm, the illumination field can be blocked using dark-field illumination or total internal reflection geometry.[1,17,34,35] Then, by adequately balancing the relative intensity of the reference and scattered fields, the contrast and intensity of the interference term can be optimized. However, digital holography and other two-arm interferometers are quite sensitive to vibrations and thermal/mechanical drift in the object or reference arms. Although the use of antivibration tables and temperature control can reduce noises and phase drifts, they introduce significant experimental constraints in many scenarios, e.g., when characterizing infectious viruses or vesicles in a biosafety cabinet. Moreover, two-arm interferometers are relatively cumbersome and require spatially and temporally coherent sources, which makes them prone to coherence artifacts, i.e., interference with parasitic reflections and scattering in the optical system also called speckle noise, thus limiting the overall quality and sensitivity of phase images.

These drawbacks are largely minimized in self-referenced QPI techniques, which can be used with an incoherent light source (LED, white light, ...) and rely on a sturdier, compact, single-arm architecture. A broad variety of common-path implementations have indeed been proposed in the past decade.[8,36−38] They give access to the wavefront shape, rather than to an absolute phase map, typically through a sampling of local wavefront gradients or curvatures. As an example, high-resolution wavefront sensors, based on, e.g., quadriwave-lateral shearing interferometry, coded aperture, or thin diffusers, can be simply used as "quantitative phase cameras", offering direct access to the scalar EM field. Unfortunately, the two conditions described above (i, dark field; ii, interferometric gain) are difficult to adapt to common path architectures since (i) some light is required even in empty places, where no particle is present, to provide a spatially

https://doi.org/10.1021/acsnano.4c05152
ACS Nano XXXX, XXX, XXX−XXX

continuous phase reference. Therefore, the zero intensity of dark-field imaging in particle-empty regions forbids self-referenced QPI measurements of the relative phase within the field of view. Also, (ii) common path methods do not give independent access to an external reference able to provide an interferometric gain. In consequence, the main strategy to increase the signal-to-noise ratio (SNR) thus consists in accumulating a large number of photons, either by averaging a large number of images[21,39] or by using a camera with a high full well capacity.[22,33] While averaging clearly decreases the temporal resolution, utilizing a high-capacity camera yields an SNR boost of the phase signal typically limited to a factor of 5 when compared to QPI performed with regular sensors.

In this article, we propose a technique coined as Z-WIM for Zernike wavefront imaging microscopy, which provides, with a single-shot acquisition, a more than 1 order of magnitude increase in sensitivity for any self-referenced QPI technique. The original Zernike phase contrast uses a dephasing and attenuating filter (classically a ring) in the Fourier plane to efficiently convert phase differences into an intensity contrast, allowing the qualitative imaging of phase features. Here, we show that the same concept can be generalized for nanoparticle imaging to boost the signal-to-noise ratio (SNR) of phase images while ensuring quantitative measurements. As such, Z-WIM offers a simple and robust way to increase the phase signals of small objects, which is adapted to modern wavefront detection schemes rather than intensity-only cameras. We present a modeling of Z-WIM and show that it allows the retrieval of quantitative phase and intensity images for the accurate and calibration-free characterization of NPs. We then present an experimental implementation with a high-resolution wavefront sensor (WFS) and demonstrate experimentally a 12× sensitivity increase.

RESULTS/DISCUSSION

Principle of Phase Amplification. Before delving into the concept of phase amplification, let us consider the measurement of the phase shift induced by a small NP using a standard QPI configuration (see Figure 1a). Here, we base our experimental applications on a common-path high-resolution wavefront sensor (quadriwave lateral shearing interferometer,[36,40,41] QLSI), but note that our reasoning holds for any wavefront imaging method. As in most QPI configurations, the sample is illuminated in transmission by a quasi-plane wave under normal incidence to facilitate dry mass estimation from optical path difference measurements as well as numerical propagation. Upon interaction with the incident field $\mathbf{E}_i$, the NP induces a scattered field $\mathbf{E}_s$. Both $\mathbf{E}_i$ and $\mathbf{E}_s$ are collected by the microscope, and the sensor receives the coherent sum of these two fields $\mathbf{E}_t = \mathbf{E}_i + \mathbf{E}_s$. These fields and their relative phase can be visualized through the use of Fresnel vectors, i.e., a representation of the scalar EM fields in the complex plane. As shown in Figure 1b, since $\|\mathbf{E}_s\| \ll \|\mathbf{E}_i\|$ for nanoparticles, the phase shift ϕ between the illumination $\mathbf{E}_i$ and the collected field $\mathbf{E}_t$ is small. As a consequence, measurements of ϕ typically yield a poor SNR (see Figure 1c) even with a shot noise-limited wavefront sensor. Recently, the advent of high-resolution QPI enabled simultaneous measurement of both the amplitude and phase of EM fields. However, in the particular case of small NPs, this raises several specific challenges, which have so far been largely overlooked, probably due to the fact that standard detectors have remained blind to phase for almost a century. The very small values of both the amplitude $|\mathbf{E}_s|$ and phase shifts ϕ are a challenge to high SNR QPI measurements.

Acknowledging the limitations of conventional strategies that involve accumulating more photons,[22,33] we propose here an approach to enhance the phase signal by selectively harvesting photons that are instrumental to the process. In the case of weakly scattering samples and (semi)spatially coherent illumination, it is well known since Frits Zernike that the contrast of phase-only objects can be enhanced by introducing $\pm\pi/2$ dephasing and attenuating filters in the Fourier plane.[42] Contributions from the nonscattered photons $\mathbf{E}_i$ and the photons scattered by the sample $\mathbf{E}_s$ can be re-equilibrated, creating high-contrast interferences when observed with an intensity detector. One well-known limitation of this phase contrast method arises when dealing with samples modulating both the amplitude and phase. Since intensity and phase contributions are entangled in the intensity variations on the detector, objects displaying both absorption and phase-shifting properties cannot be characterized quantitatively: while of course extremely effective, Zernike phase contrast remains a qualitative phase sensing technique. Noteworthily, Zernike phase contrast exploits the fact that the illumination and the light scattered by small objects can be very different in terms of angular distribution. This is especially pronounced when the illumination is a collimated, spatially coherent beam, since NP scattering covers a broad angular range, almost isotropic in the Rayleigh regime for subwavelength nano-objects. Thus, in the Fourier plane, i.e., the back focal plane of the objective, the spatially coherent illumination $\mathbf{E}_i$ is confined at the center, whereas the scattered light $\mathbf{E}_s$ can cover the entire pupil (see inset in Figure 1a).

Here, we propose to use a partially opaque filter, positioned in the pupil plane, to selectively attenuate and phase-shift the incident field $\mathbf{E}_i$ while preserving most of the scattered light $\mathbf{E}_s$. This enhances both the measurement of the amplitude (by enhancing the relative contribution of the scattered light and, therefore, the use of detector dynamics) and, most crucially, of the phase by increasing the relative phase between $\mathbf{E}_s$ and the illumination field after attenuation $\mathbf{E}_i'$. We show that this enhanced phase ϕ' can be measured with a noticeably higher SNR compared to a standard QPI system. In turn, this raises the challenge of quantitatively retrieving the original, unamplified value of the phase ϕ, a problem that we address using a simple model described below. This configuration, coined as Z-WIM for Zernike wavefront imaging microscopy, can thus be seen as a counterpart of Zernike phase contrast,[42] adapted to any quantitative phase camera or wavefront sensing method.

When a semiopaque filter with a radius R_{filter} and a complex transmission $t = t_0 e^{-i\beta}$ (with $t_0 \in \mathbb{R}^+$) is positioned at the center of the Fourier plane, the incident and scattered fields become $\mathbf{E}_i'$ and $\mathbf{E}_s'$. Since $\mathbf{E}_i$ converges at the center of the pupil for a spatially coherent source, it is attenuated and phase-shifted by a factor t: $\mathbf{E}_i' = t \cdot \mathbf{E}_i$. Conversely, the scattered field $\mathbf{E}_s$ is spread over the entire pupil plane for an isotropic scatterer and is only attenuated by a factor $(1 - t_0)\frac{R_{\text{filter}}^2}{R_{\text{pupil}}^2}$, with R_{pupil} being the pupil radius. Considering a transmission $t_0^2 \approx 1\%$ and a ratio $\frac{R_{\text{filter}}}{R_{\text{pupil}}} < 10\%$, this attenuation remains smaller than 1%, and we can thus safely consider $\mathbf{E}_s' \approx \mathbf{E}_s$ (see Supplementary Section 1). The total EM field, after interaction with the filter, then writes:

https://doi.org/10.1021/acsnano.4c05152
ACS Nano XXXX, XXX, XXX−XXX

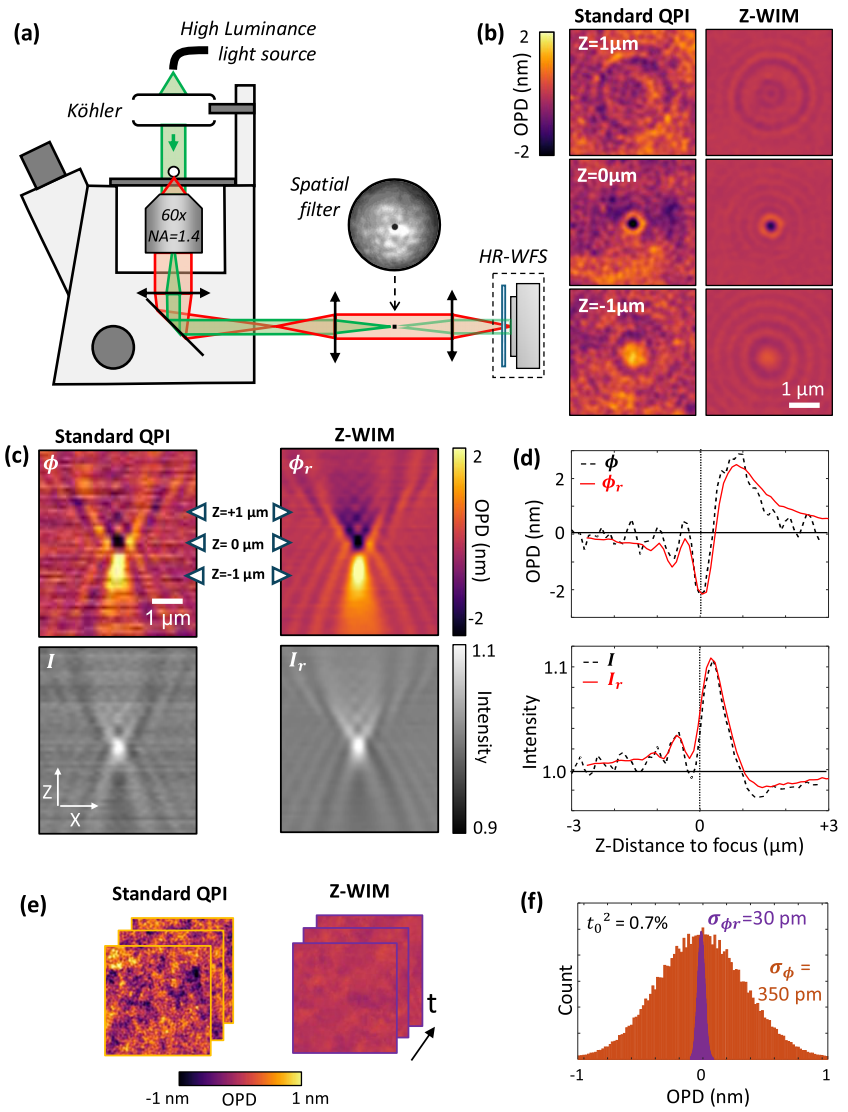

Figure 2. (a) Schematics of the experimental setup. HR-WFS: high-resolution wavefront sensor. (b) *XY* phase images of a single 100 nm NP at a glass/water interface at different *Z* around focus, (c) *XZ* cuts of these *Z* stacks (dotted lines indicate the images in b) and (d) corresponding cross sections along the *Z* axis (dotted line: standard QPI; continuous line: Z-WIM). Quantitativity is maintained even when the NP is out of focus. (e) Phase images observed over time. (f) Distribution and standard deviation of the OPD of standard QPI (orange) and Z-WIM (purple) phase images using a filter with $t_0^2 = 0.7\%$ and $\beta = 0.21$ rad.

$$\mathbf{E}_t' = \mathbf{E}_i' + \mathbf{E}_s' \approx t_0 e^{-i\beta}\mathbf{E}_i + \mathbf{E}_s \tag{1}$$

With a proper choice of t_0 and β, the relative phase ϕ' between the filtered fields $\mathbf{E}_i'$ and $\mathbf{E}_s$ can therefore be much larger than the phase ϕ obtained without filtering, as illustrated in Figure 1e. Since the phase measurement noise σ_ϕ is similar in both cases, this provides an effective improvement of the SNR of the phase measurement, as illustrated in Figure 1g,h. However, it is important to emphasize that extracting metrological values of NPs such as polarizability or dry mass from the filtered images (I', ϕ') is not as straightforward as in a standard QPI regime.

In this context, a reconstruction process is needed for estimating the values (I, ϕ) that would have been obtained in the absence of filtering. Traditional deconvolution-based approaches for image reconstruction are known to be computationally demanding, prone to amplify noises, and reliant on regularization techniques that can compromise the image's frequency content and introduce artifacts. As an alternative, we propose a direct reconstruction method based on a straightforward analytical expression. According to eq 1, the complex fields without and with filtering are indeed related through:

$$|\mathbf{E}_t|e^{-i\phi} \approx |\mathbf{E}_t'|e^{-i(\phi'+\beta)} + (1 - t_0 e^{-i\beta})|\mathbf{E}_i|$$

Experimentally, we do not have direct access to the absolute amplitude of the field but to the relative intensities, defined as $I = |\mathbf{E}_t|^2/|\mathbf{E}_i|^2$ and $I' = |\mathbf{E}_t'|^2/|\mathbf{E}_i'|^2 = |\mathbf{E}_t'|^2/t_0^2|\mathbf{E}_i|^2$. We can thus write:

$$\sqrt{I}\,e^{-i\phi} \approx t_0\sqrt{I'}\,e^{-i(\phi'+\beta)} + 1 - t_0 e^{-i\beta} \tag{2}$$

Using this relation, the intensity and phase images (I, ϕ) can be directly estimated from the filtered images (I', ϕ'). Since the filtered images (I', ϕ') benefit from an improved SNR, the retrieved images (I_r, ϕ_r) also inherit this improved SNR. As shown in Figure 1i, this yields noticeably improved quantitative phase images as compared to classical QPI. This SNR improvement (Γ_{SNR}) can be quantified in the case of very small NPs (see Figure SI3 for detailed computation), which satisfy $I' \approx 1$ and $\phi' \ll 1$ and leads to:

https://doi.org/10.1021/acsnano.4c05152
ACS Nano XXXX, XXX, XXX−XXX

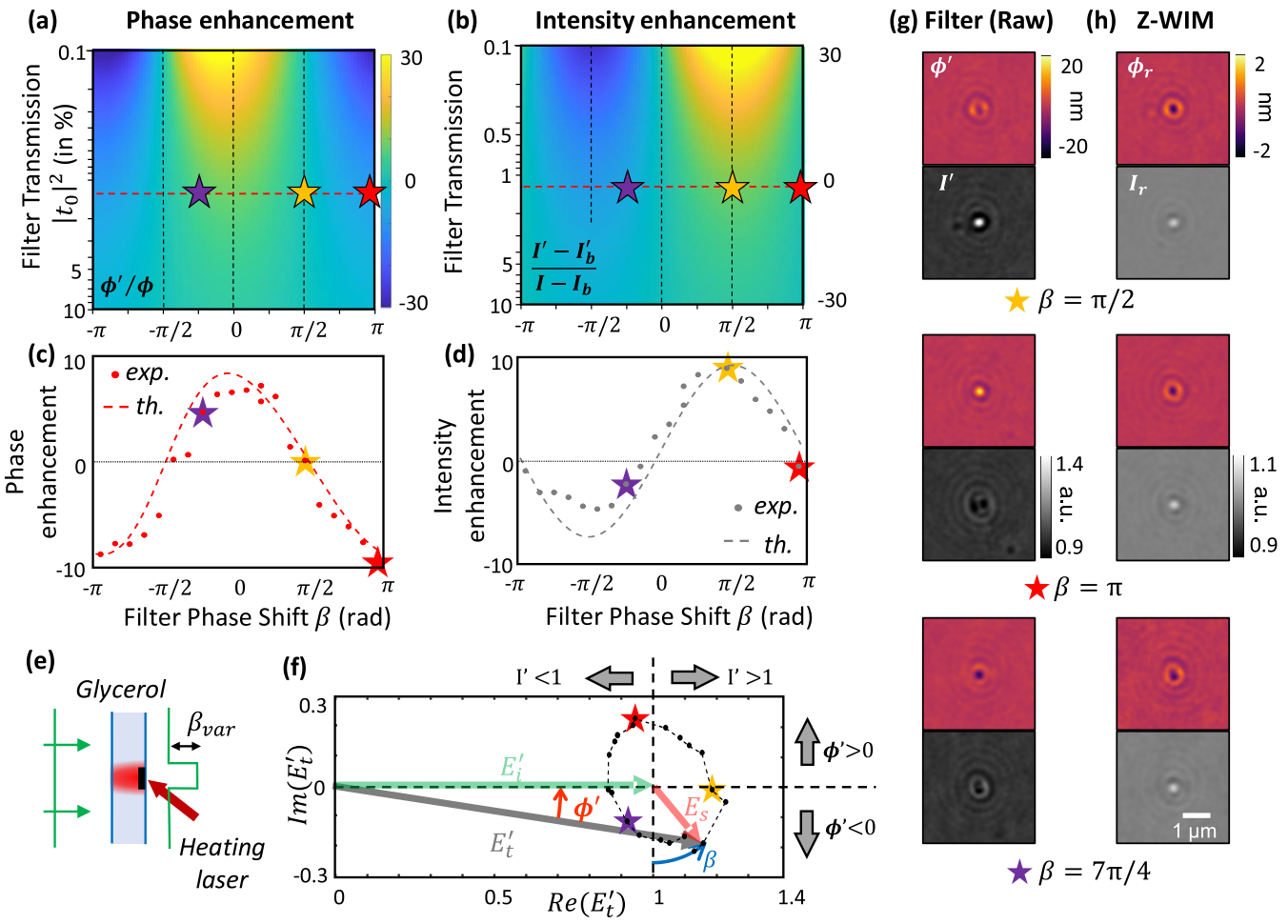

Figure 3. (a, b) Theoretical phase and intensity enhancements as a function of the filter parameters for a small dielectric NP. (c, d) Cross section of panels (a) and (b) for a filter transmission $t_0^2 = 1.5\%$. The points correspond to experimental measurements, and the stars correspond to the images in panel (g). (e) Principle of the thermally adjustable phase shift β. (f) Complex plane representation showing the effect of varying β. (g) Raw filtered images of 100 nm polystyrene beads in water measured for different values of β and (h) corresponding reconstructed images.

$$\Gamma_{SNR} = \frac{1}{t_0}\frac{1}{\sqrt{K^2\sin^2(\beta) + \cos^2(\beta)}} \quad (3)$$

with K, a constant that only depends on the properties of the QPI imaging system and represents the ratio between its intensity noise and phase noise. The use of a $t_0^2 = 1\%$ ($\beta = 0$) filter thus enables a 10-fold increase in sensitivity. Noteworthily, such a filtering strategy, even when paired with a standard camera featuring conventional full well capacity (typ. FWC = 40 ke$^-$), can result in an SNR gain that is approximately twice larger than what would be achieved with a state-of-the-art high FWC camera (FWC = 2000 ke$^-$).[22]

Importantly, this sensitivity enhancement does not depend on NP properties or dimensions. It holds true for NPs typically smaller than a few hundred nanometers of diameter (see Supplementary Section 2), thus making Z-WIM highly suitable for the blind characterization of unknown NP mixtures, including viruses and extracellular vesicles.

Experimental Validation on Calibrated Polystyrene NPs. To experimentally demonstrate a sensitivity increase with Z-WIM, we used the experimental setup based on an inverted optical microscope, and it is depicted in Figure 2a. To obtain the best results, the light source should have both a high spatial coherence and low temporal coherence. The high spatial coherence allows an efficient confinement of the incident field in the pupil plane and, thus, an efficient spatial filtering. The low temporal coherence exploits the benefits of self-referenced QPI, i.e., reducing coherence artifacts such as speckle noise. However, the relative spectral bandwidth $\Delta\lambda/\lambda$ must remain limited (typ. $\frac{\Delta\lambda}{\lambda} < 10\%$) for valid numerical repropagation of the scalar EM field over a large z range. Additionally, to allow imaging at sufficient frame rates for NP tracking despite the attenuation by the filter, the light source should have a luminance about 100 times higher in Z-WIM than in standard QPI. These requirements can be fulfilled using, e.g., a supercontinuum laser combined with a bandpass filter or a super luminescent diode (see details in Methods/Experimental Section). Because the pupil plane lies inside the collection objective, Fourier-plane filtering is performed outside the microscope by positioning a semiopaque filter of complex transmission $t = t_0 e^{-i\beta}$ precisely at the center of the reimaged pupil plane. After this Fourier-plane filtering, the sample is imaged onto a custom-made high-resolution wavefront sensor (WFS) based on QLSI[43] and described in Methods/Experimental Section.

We first characterized samples of known size and optical properties, large enough to provide a good SNR with both Z-WIM and standard QPI, to quantitatively compare these methods (Figure 2). With 100 nm-diameter polystyrene (PS)

https://doi.org/10.1021/acsnano.4c05152
ACS Nano XXXX, XXX, XXX−XXX

beads (fluospheres, Invitrogen) in water (Δn = 0.26), the expected optical path difference (OPD) signal is around 2 nm (Figure 1c), i.e., above the sensitivity ($\sigma_\phi \simeq$ 350 pm in OPD, i.e., 4.8 mrad in phase) of our standard QPI sensor without a semiopaque filter. One of the significant advantages of QPI lies in its ability to characterize NPs in solution through direct (non-iterative) numerical refocusing of defocused objects. We therefore characterized the robustness of Z-WIM against defocus by imaging these NPs both at focus and with a defocus ranging from $Z = -3$ μm to $Z = +3$ μm.

The resulting XY images and XZ cuts with and without Z-WIM filtering are shown in Figure 2b,c, aside with the corresponding cross sections along the Z direction (Figure 2d). These results show that Z-WIM, like standard QPI techniques, enables quantitative imaging even for large defocus while keeping an improved signal-to-noise ratio. This results in an exquisite reduction and flattening of the background. Z-WIM can therefore be used to quantitatively characterize smaller NPs in solution and/or, equivalently, to detect NPs over an extended Z-range as compared to standard QPI.

To quantitatively characterize the SNR improvement Γ_{SNR}, we recorded the temporal phase variation observed over 100 measurements in an area free of NPs (Figure 2e). For single-shot acquisition, the phase noise is reduced from σ_ϕ = 350 pm (4.8 mrad) with standard QPI to σ_{ϕ_r} = 30 pm (0.4 mrad) with Z-WIM (Figure 2f). The associated SNR improvement Γ_{SNR} = 12 is consistent with the theoretical expectation (eq 3) for a t_0^2 = 0.7% and $\beta \approx 0$ filter.

Effect of the Filter Properties. As discussed in Principle of Phase Amplification in Wavefront Imaging, the value of the phase shift β introduced by the filter has an important influence on the phase and intensity enhancements. Simulations carried out for various filter parameters in Figure 3a,b show that some value of β can even lead to ϕ' canceling out. Fabricating filters with different β while keeping the same t_0 to validate this experimentally can be challenging and would not allow a continuous tuning of the phase shift. Here, we implement a photothermal phase modulator inspired by ref 44 and whose experimental fabrication is described in Methods/Experimental Section to adjust the phase shift between the illumination field and the scattered field.

Experimentally, we retrieved that varying β has an effect on both the filtered phase and intensity images, as illustrated in Figure 3g. For instance, we observe a periodic inversion of the sign of both the phase and intensity contrast, as shown in Figure 3c,d. This phenomenon is observed experimentally (represented by dots) and is predicted by our model (indicated by the dashed line).

To understand this behavior, it can be convenient to consider the Fresnel vectors (Figure 3f). Here, for the sake of clarity, we keep $\mathbf{E}_i'$ aligned with the real axis and apply the relative phase shift β to the scattered field $\mathbf{E}_s$ rather than $\mathbf{E}_i$. The relation between the fields then becomes:

$$|\mathbf{E}_t'|e^{-i\phi'} = t_0|\mathbf{E}_i| + \mathbf{E}_s e^{+i\beta}$$

A change in the value of β amounts to a rotation of $\mathbf{E}_s$ around $t_0|\mathbf{E}_i| = \mathbf{E}_i'$. Therefore, as β is varied and as $\mathbf{E}_s$ rotates around $\mathbf{E}_i'$, the measured field $\mathbf{E}_t'$ repeatedly crosses the real axis, corresponding to a sign change of the phase, or the $|\mathbf{E}_t'|/|\mathbf{E}_i'| = 1$ circle corresponding to the inversions of the intensity contrast.

Using the appropriate values of β, each of the raw images in Figure 3g can therefore be processed using our analytical model to retrieve the reconstructed Z-WIM images shown in Figure 3h. As expected, all the reconstructed images are identical, which validates our approach and confirms the possibility to reconstruct directly interpretable QPI images for any value of β.

The periodic inversion of the sign of the phase however raises interesting questions regarding the SNR of the reconstructed phase images, in particular when the filtered phase ϕ' cancels out. To investigate on this, we carried out experimental and theoretical studies of the evolution of the reconstructed phase noise σ_{ϕ_r} with β. Experimental measurements (Figure 4a and

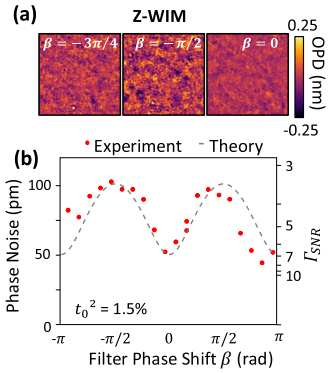

Figure 4. (a) Experimental Z-WIM images obtained for different β values considering a filter with the transmission t_0^2 = 1.5% and variable β. (b) Experimental evolution (dots) of the reconstructed phase noise σ_{ϕ_r} with β and comparison with the theoretical estimation provided in eq 3 (dotted line).

dots in Figure 4b) show that σ_{ϕ_r} critically depends on β, varying from 50 pm when $\beta = 0[\pi]$ to 100 pm when $\beta = \pi/2[\pi]$. This noise nonetheless remains consistently lower than the phase noise σ_ϕ = 350 pm of standard QPI. These results show that a quantitative reconstruction with improved sensitivity in Z-WIM can be achieved for any filter parameters t_0 and β, and the knowledge of these parameters is sufficient to ensure a quantitative reconstruction with enhanced sensitivity.

These experimental variations of σ_{ϕ_r} with β are well reproduced by our theoretical model (dashed lines in Figure 4b) described in detail in Supplementary Section 3 and whose main result is recalled in eq 3. A critical information carried by the model is that σ_{ϕ_r}, and therefore $\Gamma_{SNR} = \sigma_\phi/\sigma_{\phi_r}$, is strictly independent of the NP properties (at least for small NPs) and only depends on the properties of both the filter and phase sensor. A deeper analysis of the model shows that the phase noise of the reconstructed image σ_{ϕ_r} depends on both the phase noise σ_ϕ and intensity noise σ_I of the sensor, but to different extents depending on β, as illustrated by the $1/\sqrt{K^2\sin^2(\beta) + \cos^2(\beta)}$ dependency of eq 3. For $\beta \approx 0[\pi]$, σ_{ϕ_r} is proportional to σ_ϕ, while for $\beta \approx \pi/2[\pi]$, it is proportional to σ_I.

This observation leads to 2 major consequences. First, even though NPs with different properties can display a maximum phase enhancement for different values of β (cf Figure 3a for a dielectric NP and Figure SI4d for a gold NP), the optimal Γ_{SNR} will be achieved for the same value of β in both cases, therefore enhancing the relevance of Z-WIM for the characterization of mixtures of NPs. Second, the optimal value of β will depend on the phase sensor and, more precisely, on the value of the parameter K. In this study, we found that for our WFS, K = 2.1

https://doi.org/10.1021/acsnano.4c05152
ACS Nano XXXX, XXX, XXX−XXX

and thus, the highest Γ_{SNR} is achieved for $\beta \approx 0$ and leads to $\Gamma_{SNR} \approx 1/t_0$.

Single-Shot Polarizability Measurements. To illustrate the benefits of such sensitivity improvements, we measured the scalar EM field of 200 nm polystyrene NPs in immersion oil (n = 1.515) to extract their polarizability α using the formalism proposed by Khadir et al.[21] Figure 5 shows results obtained for

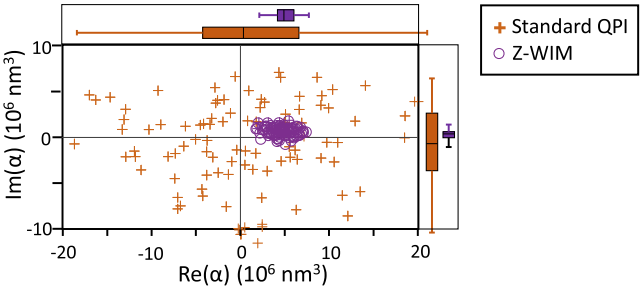

Figure 5. Polarizability of a 200 nm polystyrene NP in immersion oil retrieved from 100 consecutive images in standard QPI and Z-WIM.

100 consecutive acquisitions with both methods. While standard QPI measurements are clearly dominated by noise for these small NPs, noticeably leading to nonphysical negative values for Im(α), Z-WIM measurements display a much-reduced dispersion and yield polarizability values in good agreement with the literature.[21]

Application to the Weighing of Small Unilammellar Vesicles. We then challenged the ability of Z-WIM to characterize biologically relevant objects, which are hardly detectable in standard QPI. As a test sample, we used small unilamellar vesicles (SUVs), which represent a model system for the extracellular vesicles (EVs) secreted by most cells and bacteria and are promising candidates for drug delivery applications.[6] SUVs typically consist in a few nm-thick lipid bilayer enclosing an aqueous solution, with outer diameters ranging from a few tens of nanometers to a few μm (Figure 6a). Because of their very small mass and refractive index mismatch with respect to their aqueous environment, their characterization in standard QPI is extremely challenging.

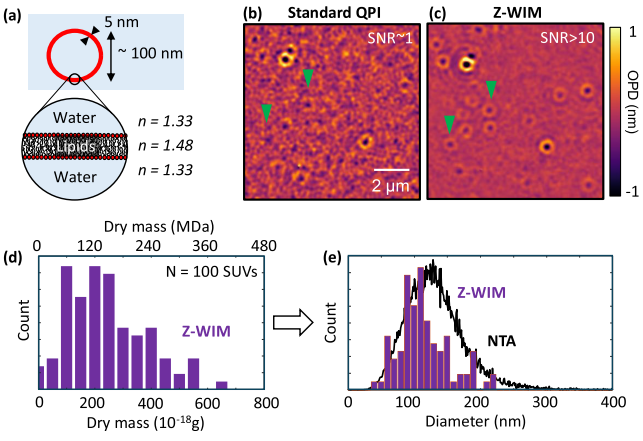

Figure 6. Phase images of 100 nm-diameter DOPC SUVs imaged in (a) standard QPI and (b) Z-WIM. (c) Schematics of a DOPC SUV. (d) Measured dry mass distribution of the SUVs and (e) estimated diameter distribution using Z-WIM (bars) compared to a commercial NTA analysis (line).

In this study, we used DOPC (1,2-dioleoyl-*sn*-glycero-3-phosphocholine) SUVs obtained by extrusion through a 100 nm pore-diameter membrane filter. Assuming a 5 nm-thick bilayer membrane, a 100 nm DOPC SUV is expected to weigh approximately 120 MDa, which amounts to an OPD of 400 pm in our configuration (N.A. = 1.4 and λ = 450 nm), very close to the typ. 350 pm detection threshold of our camera in standard QPI (Figure 6b).

With Γ_{SNR} > 10, Z-WIM enables the detection of such SUVs with an SNR > 10 (Figure 6c), thus allowing a precise weighing of individual vesicles. Here, the dry mass of the vesicles retrieved from the phase images yields an average value of 115 ± 10 MDa (Figure 6d), in good agreement with the expected value and with the dry mass retrieved from averaged standard QPI images (see Supplementary Section 5 and Figure SI8). From this dry mass, the diameter of each individual SUV can be estimated, still assuming a 5 nm-thick bilayer and a refractive index of 1.48 for DOPC[45] (bars in Figure 6e), and compared to nanoparticle tracking analysis (line in Figure 6e) hydrodynamic size estimations obtained with a commercial device (Nanosight). Both distributions are very similar, and the slight differences can be attributed to the uncertainty in the modeling of the refractive index of the SUV.

From these experiments carried out in a biological context, we infer a single-shot acquisition sensitivity of 10 MDa for Z-WIM using a standard camera-based WFS (full well capacity, ~40 ke$^-$). This is below the mass of most viruses or extracellular vesicles, which makes Z-WIM a promising and simple tool for the label-free characterization of extremely small biological entities.

CONCLUSIONS

In this article, we reported a Fourier-plane filtering technique, Z-WIM, which enables a more than 1 order of magnitude sensitivity improvement when imaging nanoparticles with self-referenced QPI while allowing quantitative measurements. We took advantage of the quasi-isotropic scattering of subdiffraction NPs to propose an artifact-free reconstruction process, which is faster and more resilient to noise as compared to more traditional deconvolutional approaches. We experimentally studied the effects of the filter parameters (transmission and phase shift) on the sensitivity increase and built upon these measurements to derive the numerical background that explains these effects and allows the easy optimization of these parameters. Altogether, we showed that even with loosely optimized filter parameters, Z-WIM represents an easy-to-implement and affordable way to increase the sensitivity of QPI.

Z-WIM can be applied to any wavefront sensor-based QPI technique (e.g., quadriwave lateral shearing interferometry[43] or diffuser-based as DiPSI[38]) and, more generally, to any self-referenced QPI technique, including multiple plane transport of intensity,[46] partitioned detection aperture,[37] ptychography,[47] *etc.* By giving quantitative access to both the phase and intensity, these techniques, and particularly Z-WIM, provide richer information on the sample as compared to intensity-only techniques such as, e.g., attenuated-COBRI.[48,49] This allows the quantitative characterization of NPs, even when out of focus, without *a priori* knowledge or calibration. In this article, we used QLSI to experimentally illustrate the potential of Z-WIM to extract quantitative properties, such as polarizability, extinction cross sections, or dry mass, of individual NPs either with higher accuracy or for otherwise undetectable NPs.

https://doi.org/10.1021/acsnano.4c05152
ACS Nano XXXX, XXX, XXX−XXX

While standard image averaging usually performs well and remains relevant with static samples, it does not allow the characterization of small NPs moving in solution. Recent approaches based on extensive image postprocessing have proven effective in this context.[22] However, they require a sufficient SNR on each individual image to enable the detection, precise 3D superlocalization, and 3D registration of the NP before averaging. While these methods can increase the precision of the measurement for rather large NPs, they do not lower the detection threshold, and small NPs remain undetectable. By increasing the sensitivity, Z-WIM allows to optimize the amount of information, which can be extracted within a given 3D field of view and is able to perform well with both static and moving samples. Of course, Z-WIM can also be combined with image averaging to push the sensitivity further, thus maximizing the amount of information that can be extracted from each nano-object. Also, numerical refocusing over extended Z-ranges can notably increase the potential number of images, which can be used for the averaging, thus increasing sensitivity for moving particles too.

Finally, the sensitivity of Z-WIM could be pushed even further if associated to a high full well capacity-based QPI sensor, or a higher attenuation coefficient filter, provided that a sufficiently bright light source is available. In this case, the sensitivity improvements should be able to reach or surpass ×100, thus enabling the label-free characterization of mobile nano-objects as small as individual proteins (100 kDa) with single-shot acquisitions and a setup of minimal complexity.

METHODS/EXPERIMENTAL SECTION

Experimental Setup. The experimental setup (Figure 2a) is based on an inverted microscope (Olympus IX-71). To meet the requirements on spatial and temporal coherence beneficial to QPI imaging, we indifferently use either a superluminescent diode (SLED EXS210014-01, Exalos) emitting at λ = 450 nm with a bandwidth $\Delta\lambda$ = 5 nm or a visible supercontinuum laser (SMHP-Visible, Leukos) combined with a bandpass filter (FBH450-40, Thorlabs) to isolate a $\Delta\lambda$ = 40 nm wavelength band centered at λ = 450 nm. Both sources are coupled into a 20 m-long multimode optical fiber (FG105LVA, Thorlabs) and collimated by an aspheric lens (f' = 4.34 mm, Thorlabs) to illuminate the sample with a plane wave with high spatial coherence (N.A. = 0.04). The high-luminance sources used in this work thus enable working in the same coherence regime as sources traditionally used in standard QLSI (LEDs, halogen lamp, ...) but provide much higher irradiance, enabling the use of short integration times. While in standard QPI, the irradiance on the sample is typically 0.5 W/cm^2, Z-WIM requires 50 W/cm^2 to achieve similar irradiance on the wavefront sensor, considering the attenuation by the filter. However, this irradiance remains below the damage threshold for living cells, which is around 1 kW/cm^2 for blue-green excitation[50,51] and below the irradiance levels used to detect NPs of similar sizes with holographic[17] or iScat techniques.[52]

The light is then collected by a 60×, N.A. = 1.4 oil immersion objective (Olympus PlanApo). The pupil plane of this objective is not directly accessible as it lies inside it and is reimaged outside the microscope using a f' = 100 mm Achromatic Doublet (Thorlabs). Fourier-plane filtering is performed in this reimaged pupil plane by either of the two filters described hereafter.

After this Fourier-plane filtering, the sample is imaged on a custom-made high resolution wavefront sensor (WFS) based on QLSI.[43] This WFS consists in a two-dimensional 20 μm-step 0−π phase-only checkerboard grating[53] (PhiMask, Idylle), reimaged a few millimeters (d = 1.6 mm) before an sCMOS camera (Andor Zyla 5.5). Here, unwanted diffracted orders are spatially filtered to keep only 4 orders thanks to a relay telescope (not shown in Figure 2a). This QLSI system yields performances comparable to those of modified Hartmann−Mask-based sensors.[22]

Description of the Spatial Filters. Most of the experiments presented in this article have been performed using a semiopaque filter for Fourier-plane filtering consisting in a 100 nm-thick gold disc deposited on a glass substrate. Its radius (R_{filter} = 100 μm) has been chosen considering the reimaged pupil radius (R_{pupil} = 2.3 mm) to obtain $\frac{R_{filter}}{R_{pupil}} < 10\%$ and thus preserve quantitativity (see Supplementary Section 1). This radius corresponds to N.A. = 0.06 in the reimaged pupil plane, i.e., slightly more than the N.A. = 0.04 of the illumination, which can therefore be blocked efficiently. The gold thickness was chosen to provide both a transmission $t_0^2 < 1\%$ and a negligible phase shift β, leading to $\Gamma_{SNR} > 10$. Using numerical simulations based on the Fresnel coefficients for a multilayered thin film,[54] we estimated that the filter induces a transmission t_0^2 = 0.7% and phase shift β = 0.21 rad. The transmission value was confirmed experimentally using transmission microscopy images of the filter (see Supplementary Section 4).

For the experiments requiring a precise control of the phase shift β, we slightly modified the previous filter. In this case, a similar 100 nm-thick, 200 μm-diameter gold disc filter is covered by a 50 μm-thick glycerol layer in a chamber sealed by a sapphire window (Figure 3e). The transmission of this filter was measured to be t_0^2 = 1.5%, which corresponds to an expected Γ_{SNR} = 8 for $\beta \approx 0$. The temperature of the filter and the value of β are controlled with a laser diode (CNI, 633 nm, 500 mW) focused on the gold disc to locally heat the gold and glycerol layers. Since the refractive index of glycerol decreases with the temperature ($\delta n/\delta T = -2.1 \times 10^{-4}$ K^{-1}), its optical thickness and, therefore, β can be precisely controlled.

ASSOCIATED CONTENT

Supporting Information

The Supporting Information is available free of charge at https://pubs.acs.org/doi/10.1021/acsnano.4c05152.

Numerical estimation of the reconstruction error in ZWIM, followed by the analytical derivations of the effects of the NP and filter properties on the phase and intensity enhancements and on the sensitivity improvement (PDF)

Phase and intensity images acquired in standard QPI and with the filter from Figure 1 and matlab code function enabling the reconstruction of quantitative phase and intensity images from the filtered images (ZIP)

AUTHOR INFORMATION

Corresponding Authors

Benoit Rogez − *Institut de la Vision, Sorbonne Université, CNRS-UMR 7210, Inserm-UMR S968, Paris 75012, France; L2n, Université de technologie de Troyes, CNRS-UMR 7076, Troyes 10004, France;* orcid.org/0000-0003-1046-5461; Email: benoit.rogez@utt.fr

Pascal Berto − *Institut de la Vision, Sorbonne Université, CNRS-UMR 7210, Inserm-UMR S968, Paris 75012, France; Université Paris Cité, Paris 75006, France; Institut Universitaire de France (IUF), Paris 75231, France;* orcid.org/0000-0003-1664-257X; Email: pascal.berto@parisdescartes.fr

Authors

Clémence Gentner − *Institut de la Vision, Sorbonne Université, CNRS-UMR 7210, Inserm-UMR S968, Paris 75012, France*

Hadrien M. L. Robert − *Institut de la Vision, Sorbonne Université, CNRS-UMR 7210, Inserm-UMR S968, Paris 75012, France*

Anis Aggoun − *Institut de la Vision, Sorbonne Université, CNRS-UMR 7210, Inserm-UMR S968, Paris 75012, France;* orcid.org/0009-0002-7283-0743

https://doi.org/10.1021/acsnano.4c05152
ACS Nano XXXX, XXX, XXX−XXX

Gilles Tessier − *Institut de la Vision, Sorbonne Université, CNRS-UMR 7210, Inserm-UMR S968, Paris 75012, France*
Pierre Bon − *Université de Limoges, CNRS, XLIM, UMR 7252, Limoges 87000, France*

Complete contact information is available at: https://pubs.acs.org/10.1021/acsnano.4c05152

Author Contributions

#C.G. and B.R. contributed equally to this work.

Funding

The project has received funding from the Agence Nationale de la Recherche (ANR-20-CE42-0006 - MaxPhase, ANR-21-CE42-0023-01 PROFIT, ANR-21-CE42-0008 ELISE) and the European Union's Horizon Research and Innovation Programme (European Research Council (ERC), grant agreement No. 848645 and No. 10106380).

Notes

The authors declare no competing financial interest.

ACKNOWLEDGMENTS

The authors thank L. Belliard for the fabrication of the gold discs and for her help in characterizing them. We also warmly thank both D. D'Arrigo and S. Mangenot for providing the SUVs.

REFERENCES

(1) Brasiliense, V.; Berto, P.; Combellas, C.; Tessier, G.; Kanoufi, F. Electrochemistry of Single Nanodomains Revealed by Three-Dimensional Holographic Microscopy. *Acc. Chem. Res.* **2016**, *49* (9), 2049−2057.
(2) Dibsy, R.; Bremaud, E.; Mak, J.; Favard, C.; Muriaux, D. HIV-1 Diverts Cortical Actin for Particle Assembly and Release. *Nat. Commun.* **2023**, *14* (1), 6945. *2023 14:1*
(3) Shi, J.; Kantoff, P. W.; Wooster, R.; Farokhzad, O. C. Cancer Nanomedicine: Progress, Challenges and Opportunities. *Nature Reviews Cancer* **2017**, *17* (1), 20−37. *2016 17:1*
(4) Chen, J.; Guo, Y.; Zhang, X.; Liu, J.; Gong, P.; Su, Z.; Fan, L.; Li, G. Emerging Nanoparticles in Food: Sources, Application, and Safety. *J. Agric. Food Chem.* **2023**, *71* (8), 3564−3582.
(5) Guerrini, G.; Magrì, D.; Gioria, S.; Medaglini, D.; Calzolai, L. Characterization of Nanoparticles-Based Vaccines for COVID-19. *Nature Nanotechnology* **2022**, *17* (6), 570−576. *2022 17:6*
(6) Panahi, Y.; Farshbaf, M.; Mohammadhosseini, M.; Mirahadi, M.; Khalilov, R.; Saghfi, S.; Akbarzadeh, A. Recent Advances on Liposomal Nanoparticles: Synthesis, Characterization and Biomedical Applications. *Artif. Cells, Nanomed., Biotechnol.* **2017**, *45*, 788.
(7) Park, Y.; Depeursinge, C.; Popescu, G. Quantitative Phase Imaging in Biomedicine. *Nat Photonics* **2018**, *12* (10), 578−589.
(8) Nguyen, T. L.; Pradeep, S.; Judson-Torres, R. L.; Reed, J.; Teitell, M. A.; Zangle, T. A. Quantitative Phase Imaging: Recent Advances and Expanding Potential in Biomedicine. *ACS Nano* **2022**, *16* (8), 11516−11544.
(9) Priest, L.; Peters, J. S.; Kukura, P. Scattering-Based Light Microscopy: From Metal Nanoparticles to Single Proteins. *Chem Rev* **2021**, *121* (19), 11937−11970.
(10) Piliarik, M.; Sandoghdar, V. Direct Optical Sensing of Single Unlabelled Proteins and Super-Resolution Imaging of Their Binding Sites. *Nat. Commun.* **2014**, *5* (1), 4495. *2014 5:1*
(11) Lindfors, K.; Kalkbrenner, T.; Stoller, P.; Sandoghdar, V. Detection and Spectroscopy of Gold Nanoparticles Using Supercontinuum White Light Confocal Microscopy. *Phys. Rev. Lett.* **2004**, *93* (3), No. 037401.
(12) Bundschuh, M.; Filser, J.; Lüderwald, S.; McKee, M. S.; Metreveli, G.; Schaumann, G. E.; Schulz, R.; Wagner, S. Nanoparticles in the Environment: Where Do We Come from, Where Do We Go To? *Environ. Sci. Eur.* **2018**, *30* (1), 6.
(13) Sonwani, S.; Madaan, S.; Arora, J.; Suryanarayan, S.; Rangra, D.; Mongia, N.; Vats, T.; Saxena, P. Inhalation Exposure to Atmospheric Nanoparticles and Its Associated Impacts on Human Health: A Review. *Frontiers in Sustainable Cities* **2021**, *3*, No. 690444.
(14) Berto, P.; Guillon, M.; Bon, P. Wrapping-Free Numerical Refocusing of Scalar Electromagnetic Fields. *Appl. Opt.* **2018**, *57* (22), 6582.
(15) Brault, D.; Olivier, T.; Soulez, F.; Joshi, S.; Faure, N.; Fournier, C. Accurate Unsupervised Estimation of Aberrations in Digital Holographic Microscopy for Improved Quantitative Reconstruction. *Opt. Express* **2022**, *30* (21), 38383.
(16) Ortiz-Orruño, U.; Jo, A.; Lee, H.; Van Hulst, N. F.; Liebel, M. Precise Nanosizing with High Dynamic Range Holography. *Nano Lett* **2021**, *21* (1), 317−322.
(17) Ortiz-Orruño, U.; Quidant, R.; van Hulst, N. F.; Liebel, M.; Ortega Arroyo, J. Simultaneous Sizing and Refractive Index Analysis of Heterogeneous Nanoparticle Suspensions. *ACS Nano* **2023**, *17* (1), 221−229.
(18) Hamilton, S.; Regan, D.; Payne, L.; Langbein, W.; Borri, P. Sizing Individual Dielectric Nanoparticles with Quantitative Differential Interference Contrast Microscopy. *Analyst* **2022**, *147* (8), 1567.
(19) Saemisch, L.; Van Hulst, N. F.; Liebel, M. One-Shot Phase Image Distinction of Plasmonic and Dielectric Nanoparticles. *Nano Lett* **2021**, *21* (9), 4021−4028.
(20) Olsén, E.; García Rodríguez, B.; Skärberg, F.; Parkkila, P.; Volpe, G.; Höök, F.; Sundås Midtvedt, D. Dual-Angle Interferometric Scattering Microscopy for Optical Multiparametric Particle Characterization. *Nano Lett* **2024**, *24* (6), 1874.
(21) Khadir, S.; Andrén, D.; Chaumet, P. C.; Monneret, S.; Bonod, N.; Käll, M.; Sentenac, A.; Baffou, G. Full Optical Characterization of Single Nanoparticles Using Quantitative Phase Imaging. *Optica* **2020**, *7* (3), 243−248. *Vol. 7, Issue 3, pp. 243−248*
(22) Nguyen, M.-C.; Bonnaud, P.; Dibsy, R.; Maucort, G.; Lyonnais, S.; Muriaux, D.; Bon, P. Label-Free Single Nanoparticle Identification and Characterization in Demanding Environment, Including Infectious Emergent Virus. *Small* **2023**, *20*, No. 2304564.
(23) Nguyen, M.-C.; Berto, P.; Valentino, F.; Kanoufi, F.; Tessier, G. Spectroscopy of Individual Brownian Nanoparticles in Real-Time Using Holographic Localization. *Optics Express* **2022**, *30* (24), 43182−43194. *Vol. 30, Issue 24, pp. 43182−43194*
(24) Nguyen, M.-C.; Berto, P.; Valentino, F.; Lemineur, J.-F.; Noel, J. M.; Kanoufi, F.; Tessier, G. 3D Spectroscopic Tracking of Individual Brownian Nanoparticles during Galvanic Exchange. *ACS Nano* **2022**, *16* (9), 14422.
(25) Barer, R. Interference Microscopy and Mass Determination. *Nature* **1952**, *169* (4296), 366−367. *1952 169:4296*
(26) Bon, P.; Bourg, N.; Lécart, S.; Monneret, S.; Fort, E.; Wenger, J.; Lévêque-Fort, S. Three-Dimensional Nanometre Localization of Nanoparticles to Enhance Super-Resolution Microscopy. *Nat. Commun.* **2015**, *6* (1), 7764. *2015 6:1*
(27) Sheng, J.; Malkiel, E.; Katz, J. Digital Holographic Microscope for Measuring Three-Dimensional Particle Distributions and Motions. *Appl. Opt.* **2006**, *45* (16), 3893−3901. *Vol. 45, Issue 16, pp. 3893−3901*
(28) Wu, T.; Guillon, M.; Gentner, C.; Rigneault, H.; Tessier, G.; Bon, P.; Berto, P. 3D Nanoparticle Superlocalization with a Thin Diffuser. *Opt. Lett.* **2022**, *47* (12), 3079.
(29) Thiele, J. C.; Pfitzner, E.; Kukura, P. Single-Protein Optical Holography. *Nature Photonics* **2024**, *18* (4), 388−395. *2024 18:4*
(30) Bouchet, D.; Dong, J.; Maestre, D.; Juffmann, T. Fundamental Bounds on the Precision of Classical Phase Microscopes. *Phys Rev Appl* **2021**, *15* (2), No. 024047.
(31) Nie, Y.; Zhou, R. Beating Temporal Phase Sensitivity Limit in Off-Axis Interferometry Based Quantitative Phase Microscopy. *APL Photonics* **2021**, *6* (1), No. 011302.
(32) Charrière, F.; Colomb, T.; Montfort, F.; Cuche, E.; Marquet, P.; Depeursinge, C. Shot-Noise Influence on the Reconstructed Phase Image Signal-to-Noise Ratio in Digital Holographic Microscopy. *Appl. Opt.* **2006**, *45* (29), 7667−7673. *Vol. 45, Issue 29, pp. 7667−7673*

(33) Yaqoob, Z.; Hosseini, P.; Zhou, R.; Peres, C.; Kuang, C.; So, P. T. C.; Diaspro, A.; Kim, Y.-H. Pushing Phase and Amplitude Sensitivity Limits in Interferometric Microscopy. *Opt. Lett.* **2016**, *41* (7), 1656−1659. *Vol. 41, Issue 7, pp. 1656−1659*
(34) Gross, M.; Warnasooriya, N.; Fournier, D.; Suck, S.; Coppey-Moisan, M.; Atlan, M.; Absil, E.; Tessier, G. Photothermal Heterodyne Holography of Gold Nanoparticles. *Optics Express* **2010**, *18* (2), 780−786. , *Vol. 18, Issue 2, pp. 780−786*
(35) Absil, E.; Tessier, G.; Fournier, D.; Gross, M.; Atlan, M. Full Field Imaging of Isolated Metallic Nano Objects. *The European Physical Journal Applied Physics* **2009**, *47* (1), 12704.
(36) Bon, P.; Maucort, G.; Wattellier, B.; Monneret, S. Quadriwave Lateral Shearing Interferometry for Quantitative Phase Microscopy of Living Cells. *Opt Express* **2009**, *17* (15), 13080.
(37) Ford, T. N.; Chu, K. K.; Parthasarathy, A. B.; Mertz, J. Quantitative Phase Imaging Using a Partitioned Detection Aperture. *Opt. Lett.* **2012**, *37* (19), 4062−4064. *Vol. 37, Issue 19, pp. 4062−4064*
(38) Berto, P.; Rigneault, H.; Guillon, M. Wavefront Sensing with a Thin Diffuser. *Opt. Lett.* **2017**, *42* (24), 5117.
(39) Bon, P.; Lécart, S.; Fort, E.; Lévêque-Fort, S. Fast Label-Free Cytoskeletal Network Imaging in Living Mammalian Cells. *Biophys. J.* **2014**, *106* (8), 1588−1595.
(40) Primot, J.; Sogno, L. Achromatic Three-Wave (or More) Lateral Shearing Interferometer. *Journal of the Optical Society of America A* **1995**, *12* (12), 2679.
(41) Baffou, G. Wavefront Microscopy Using Quadriwave Lateral Shearing Interferometry: From Bioimaging to Nanophotonics. *ACS Photonics* **2023**, *10*, 322.
(42) Zernike, F. Phase Contrast, a New Method for the Microscopic Observation of Transparent Objects Part II. *Physica* **1942**, *9* (10), 974−986.
(43) Primot, J.; Guérineau, N. Extended Hartmann Test Based on the Pseudoguiding Property of a Hartmann Mask Completed by a Phase Chessboard. *Appl. Opt.* **2000**, *39* (31), 5715−5720. *Vol. 39, Issue 31, pp. 5715−5720*
(44) Robert, H. M. L.; Holanová, K.; Bujak, Ł.; Vala, M.; Henrichs, V.; Lánský, Z.; Piliarik, M. Fast Photothermal Spatial Light Modulation for Quantitative Phase Imaging at the Nanoscale. *Nat. Commun.* **2021**, *12* (1), 2921. *2021 12:1*
(45) Parkkila, P.; Elderdfi, M.; Bunker, A.; Viitala, T. Biophysical Characterization of Supported Lipid Bilayers Using Parallel Dual-Wavelength Surface Plasmon Resonance and Quartz Crystal Microbalance Measurements. *Langmuir* **2018**, *34* (27), 8081−8091.
(46) Teague, M. R. Deterministic Phase Retrieval: A Green's Function Solution. *JOSA* **1983**, *73* (11), 1434−1441. *Vol. 73, Issue 11, pp. 1434−1441*
(47) Rodenburg, J. M.; Humphry, M. J.; Maiden, A. M. Optical Ptychography: A Practical Implementation with Useful Resolution. *Opt. Lett.* **2010**, *35* (15), 2585−2587. *Vol. 35, Issue 15, pp. 2585−2587*
(48) Cheng, C. Y.; Liao, Y. H.; Hsieh, C. L. High-Speed Imaging and Tracking of Very Small Single Nanoparticles by Contrast Enhanced Microscopy. *Nanoscale* **2019**, *11* (2), 568−577.
(49) Huang, Y. F.; Zhuo, G. Y.; Chou, C. Y.; Lin, C. H.; Chang, W.; Hsieh, C. L. Coherent Brightfield Microscopy Provides the Spatiotemporal Resolution to Study Early Stage Viral Infection in Live Cells. *ACS Nano* **2017**, *11* (3), 2575−2585.
(50) Linarès-Loyez, J.; Ferreira, J. S.; Rossier, O.; Lounis, B.; Giannone, G.; Groc, L.; Cognet, L.; Bon, P. Self-Interference (SELFI) Microscopy for Live Super-Resolution Imaging and Single Particle Tracking in 3D. *Front. Phys.* **2019**, *7*, 68.
(51) Waldchen, S.; Lehmann, J.; Klein, T.; Van De Linde, S.; Sauer, M. Light-Induced Cell Damage in Live-Cell Super-Resolution Microscopy. *Sci. Rep.* **2015**, *5*, 15348.
(52) Kukura, P.; Ewers, H.; Müller, C.; Renn, A.; Helenius, A.; Sandoghdar, V. High-Speed Nanoscopic Tracking of the Position and Orientation of a Single Virus. *Nat Methods* **2009**, *6* (12), 923−927.
(53) Bon, P.; Linarès-Loyez, J.; Feyeux, M.; Alessandri, K.; Lounis, B.; Nassoy, P.; Cognet, L. Self-Interference 3D Super-Resolution Microscopy for Deep Tissue Investigations. *Nature Methods* **2018**, *15* (6), 449−454. *2018 15:6*
(54) Rogez, B.; Marmri, Z.; Thibaudau, F.; Baffou, G. Thermoplasmonics of Metal Layers and Nanoholes. *APL Photonics* **2021**, *6* (10), No. 101101.

https://doi.org/10.1021/acsnano.4c05152
ACS Nano XXXX, XXX, XXX−XXX